Compaction Banding in High-Porosity Carbonate Rocks: 1. Experimental Observations

Youssouf Abdallah, Jean Sulem, Michel Bornert, Siavash Ghabezloo, Ioannis Stefanou

Compaction Banding in High Porosity Carbonate Rocks: 1. Experimental Observations

Youssouf Abdallah[1], Jean Sulem[1], Michel Bornert[1], Siavash Ghabezloo[1], and Ioannis Stefanou[2]

[1] *Laboratoire Navier, École des Ponts ParisTech, Univ. Gustave Eiffel, CNRS, Marne-la-Vallée, France*
[2] *École Centrale de Nantes, Université de Nantes, CNRS, GeM (Institut de Recherche en Génie Civil et Mécanique), Nantes, France*

Published online on January 2021

To cite:
Abdallah, Y., Sulem, J., Bornert, M., Ghabezloo, S., & Stefanou, I. (2021). Compaction banding in high porosity carbonate rocks: 1. Experimental observations. Journal of Geophysical Research: Solid Earth, 126, e2020JB020538. https://doi.org/10.1029/2020JB020538

Keypoints

- Computed tomography and digital volume correlation are efficient tools to identify the formation and type of deformation bands in limestone samples.
- The porosity heterogeneity controls the onset and propagation of compaction bands.
- Calcite grain crushing is dominant in high porosity zones whereas intergranular cement cracking occurs in low porosity zones.

Abstract

Identifying the mechanisms that control the formation of compaction bands is of high interest in reservoir mechanics since these structures may drastically affect the performance of geosystems operations. Considering the difficulty to identify compaction bands in carbonate samples tested in the laboratory, the Digital Volume Correlation (DVC) technique is applied here and proves to be a relevant method. X-Ray Computed Tomography (XRCT) images of Saint Maximin limestone (SML) centimetric samples are recorded before and after several triaxial loading stages and deformation maps are built. A new post-processing method based on the analysis of the kinematics throughout the observed localization bands is proposed to identify their type. Compaction bands are identified at relatively high-confining pressures, while shear bands are observed at lower confinements. The brittle-ductile transitional regime reveals the formation of compactive shear bands, while a diffuse compaction is observed under hydrostatic loading. The effect of porosity heterogeneities on strain localization is explored by computing 3D porosity maps from calibrated XRCT images. Compaction bands are found to dominantly lay inside high-porosity zones, while shear bands can cross both high- and low-porosity zones. The band orientation is found to be controlled primarily by the confining pressure. Moreover, the porosity heterogeneity strongly affects the volumetric behavior inside the deformation bands, with a dilatant behavior identified in low-porosity zones in contrast to a compactive behavior observed in high-porosity zones. Finally, Scanning Electron Microscopy (SEM) observations reveal that calcite grain crushing is dominant in high-porosity zones, while intergranular cement cracking occurs in denser zones.

1 Introduction

Understanding the inelastic compaction of sedimentary rocks is highly important to enhance the performance of various geosystem operations. This compaction may occur in a homogeneous or localized form, such as compaction bands which are often reported in sandstone formations in the literature (e.g. Sternlof et al. (2005); Eichhubl et al. (2010)), but also in limestones (e.g. Tondi et al. (2006); Rath et al. (2011)). A reduction in the pore space is generally observed inside the compaction bands leading to a permeability reduction of several orders of magnitude in comparison with the host rock (Fossen et al., 2011). Consequently, the performance of fluid reservoirs and waste storage geosystems may be drastically affected (e.g. geothermal energy (Barbier, 2002); CO_2 storage (Rutqvist, 2012); oil and gas production (Olsson et al., 2002); see also Holcomb et al. (2007)). Moreover, strain localization bands are generally associated with instability phenomena due to material alteration and strength reduction. When fluids are present, the volume changes may affect the pore pressure and subsequently the effective stress state. Furthermore, chemical interactions can occur between reactive fluids and the solid matrix, such as the dissolution/precipitation of quartz and calcite minerals in water (Grgic, 2011). The material comminution inside the bands leads to an increase of the specific surface of the solid phase and thus of the interacting surface between the reactive fluid and the material, which causes the acceleration of the chemical reactions and contributes in a further degradation of the material. A positive feedback process can take place leading to a mechanical instability (Ciantia and Hueckel, 2013; Stefanou and Sulem, 2014).

Carbonate rocks represent a large category of sedimentary rocks. According to Flügel (2013), carbonate rocks hold 40% to 60% of oil and gas reserves around the world. In laboratory studies, the inelastic deformation and compaction banding in carbonate rocks have been less investigated than in sandstones. In addition to the great variety of carbonate rock microstructures (Dunham, 1962; Choquette and Pray, 1970), the experimental characterization of compaction bands in carbonate rock samples is generally more challenging than in sandstone samples. First of all, identifying deformation bands by eye inspection of sample surfaces is not obvious for limestones (Baud et al., 2017b), unlike for sandstones (Baud et al., 2004; Fortin et al., 2006). Second, although microscopic observations on thin sections can give a qualitative description of the micromechanisms involved in strain localiza-

tion, they do not allow to characterize the 3D pattern of compaction bands neither their evolution with loading. Surface observation by means of both optical and electron microscopy of Estaillades carbonate rocks submitted to mechanical load have been performed by Dautriat et al. (2011) at several scales. The processing of the images by digital image correlation permitted to evidence various active deformation mechanisms. Such a methodologgy is however limited to uniaxial loading conditions without confinement, which might not be fully representative of the actual mechanisms in geological systems. On the other hand, a number of experimental techniques such as acoustic emission measurements and quantitative microstructural analyses allowing to evaluate crack densities (e.g. (Wu et al., 2000; Otani et al., 2005)) have permitted to successfully identify compaction bands in sandstones (Baud et al., 2004; Fortin et al., 2006), but have failed in carbonate rocks (Vajdova et al., 2004, 2010). This can be linked to the fact that the micromechanisms of deformation involved in compaction banding are not the same in sandstones and in limestones (Zhu et al., 2010; Abdallah, 2019). In this study, the Digital Volume Correlation (DVC) technique (Bay et al., 1999) is adopted for identifying compaction banding in limestones. This technique has been successfully applied to many materials such as bone materials (Follet et al., 2005), argillaceous rocks (Lenoir et al., 2007) and carbonate rocks (Zinsmeister, 2013; Ji et al., 2014; Papazoglou et al., 2017). It permits to characterize the 3D pattern of a strain localization band, follow its evolution with loading and describe the deformation inside the band.

The identification of the deformation band types is usually made indirectly as the analyses are based on observations performed at the state after strain localization. The band type is deduced from its orientation with respect to the principal stress direction. However, a more accurate identification of the band type requires an evaluation of the ratio between shear and compaction displacement offset Wu et al. (2020). In this study, a simple and original method that operates on the data of the strain maps obtained from DVC is proposed.

On another hand, how the microstructural features control compaction banding remains unclear. At sample scale, compaction bands are identified in many sedimentary rocks, but homogeneous cataclastic flow occurs in others (Wong and Baud, 2012). According to Rustichelli et al. (2012), a high macroporosity is a key factor to enhance pore collapse and induces compaction bands whereas the abundance of cement between grains can limit the stress concentration (Aydin et al., 2006). Baud et al. (2017b) studied

two facies of Leitha limestone having the same mineralogical composition and grain size distribution. They concluded that cementation has a negative impact on compaction bands formation. Furthermore, micropores do not seem to affect the deformation mode as they remain intact after strain localization (Rath et al., 2011). In addition, a poor grain sorting can inhibit the formation of deformation bands as large grains can play the role of barriers to localization propagation Cheung et al. (2012). Because of the large variety of the microstructural features of carbonate rocks, more studies are required to understand the impact of the microstructure heterogeneity on compaction banding. The aim of the present study is to contribute to a better understanding of this impact. In this objective, 3D maps of the local porosity evaluated at some meso-scale are computed from suitably calibrated X-Ray Computed Tomography (XRCT) images of the samples recorded at different deformation states and compared against the strain maps obtained from DVC at a comparable local scale. In addition to the XRCT images for which the resolution is limited to a voxel size of $24 \times 24 \times 24$ μm^3, thin sections of the rock in its initial and deformed states are prepared and observed using Scanning Electron Microscopy (SEM) in order to investigate the deformation mechanisms involved inside the strain localization bands. These observations have been performed at the *Laboratoire de Géologie* of *Ecole Normale Supérieure* (Paris) and at the *Laboratoire de Mécanique des Solides* of *Ecole Polytechnique* (Palaiseau).

2 Material Description

The Saint-Maximin limestone (SML), a porous rock from the Parisian basin (Fronteau et al., 2010), is selected in this study. The rock has been provided by the Rocamat quarry in Saint-Maximin-sur-Oise in the North of Paris. Cylindrical samples of 4 cm in diameter and 8 cm in height have been cored. The interconnected porosity of SML, measured by the hydrostatic weighing method on 72 cylindrical samples, has a mean value of 37.9%. According to Baud et al. (2017a), calcite amounts to about 80% of the solid mass, while quartz grains represent the remainder.

Laboratory XRCT images of the SML samples recorded in their undeformed state, systematically show a microstructural heterogeneity at the centimetric scale. The details of the imaging technique will be presented later in Section 3.2. Figure 1 shows a typical transverse cross-section of the

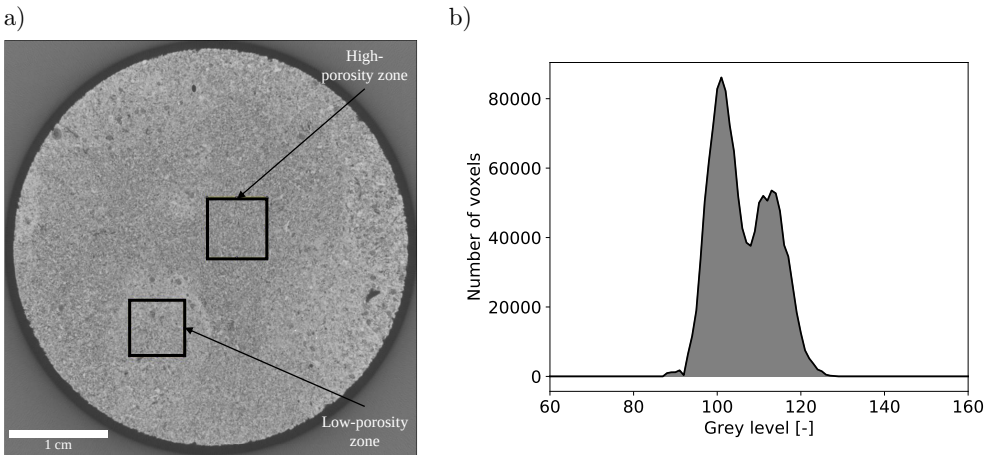

Figure 1: **a)** A typical transverse cross-section of an 8-bit XRCT image of a SML sample in its initial state. The black squares indicate the locations of two cored cubic specimens on which mercury intrusion porosimetry is conducted; **b)** The corresponding grey level histogram.

XRCT images and its corresponding grey level histogram. An alternation between high-porosity and low-porosity zones, corresponding respectively to darker and brighter areas in the images, is observed. In addition, isolated large pores (up to 2 mm in diameter) are commonly observed inside the low-porosity zones. These pores are not close to each other and do not seem to form connected porosity clusters.

To characterize the microstructural attributes at grain scale in both zones, a thin section of a sample impregnated with blue epoxy resin is prepared and observed with SEM in backscattered electron mode. Figure 2 shows an interface between the two zones. In the denser zones, grains are larger and more cemented than in the more porous ones. In addition, the microscopic observations performed on the sample at the initial state suggest that the microstructure is quite isotropic and no bedding orientation could be detected.

In order to characterize the porosity of each zone, four cubic specimens, with a side length of around 6 mm, are selected on the XRCT images and cored using a wire saw (the location of two such specimens is shown in Figure 1). Mercury intrusion porosimetry is performed on these specimens and the obtained porosity distributions are plotted in Figure 3. The specimens referred to as D1, D2 and D3 are prepared from denser zones, while the sample

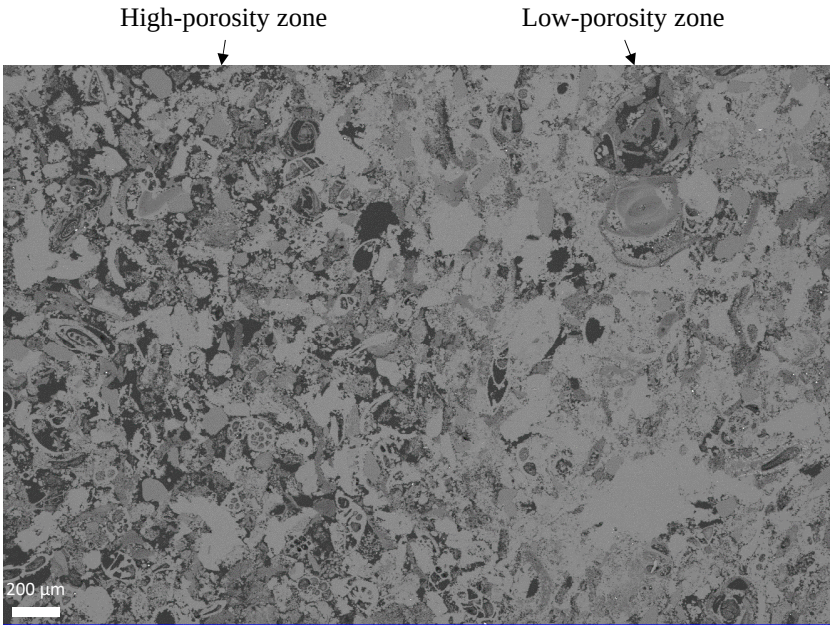

Figure 2: SEM observation (BSE mode) of a thin section showing an interface between high- and low-porosity zones.

Table 1: Porosity of the four cubic $6 \times 6 \times 6$ mm^3 specimens as evaluted by mercury intrusion porosimetry: micro- and macro-porosities are calculated assuming that 0.6 μm is the threshold size separating the two families.

Zone	Specimen	ϕ_{micro}	ϕ_{macro}	ϕ_{total}
Low-porosity	D1	8.8%	26.5%	35.3%
Low-porosity	D2	9.1%	21.4%	30.5%
Low-porosity	D3	8.4%	26.8%	35.2%
High-porosity	P1	9.7%	30.9%	40.6%

referred to as P1 is cored from a more porous zone. The four porosimetry curves exhibit a bimodal shape. The micropores have throat diameters ranging from 0.04 μm to about 1 μm, with a peak at around 0.2 μm. As for the macropores, their diameters range from about 1 to 20 μm with a strong predominance of pores around 10 μm. These larger pores are significantly more abundant in high-porosity zones. Their lower proportion corroborates the statement of a higher cementation in low-porosity zones. The microporosity is attributed to the pores inside the calcite grains whereas the macroporosity represents the intergranular pores and those associated with shells (see Figure 2). It is worth mentioning that this distribution of pore diameters is very comparable to the one of the Estaillades limestone studied by Dautriat et al. (2011), but that the pores in the carbonate rocks studied by Baechle et al. (2008) and Zhu et al. (2010) were much larger as the threshold between micro- and macro-porosity was observed to be around 30 μm.

The total, micro- and macro-porosities of the four specimens are evaluated assuming that 0.6 μm is the pore size threshold between the two families. The results are given in Table 1. It is observed that the porosity varies from less than 35% in the denser zones to more than 40% in the more porous zones. The micro-porosity ranges from 8.4% to 9.7% for all samples and thus seems to be quite uniform, so that the heterogeneity of the total porosity is essentially due to the variations of the macro-porosity. Such porosity heterogeneity is not surprising in carbonate rocks. Indeed, Baud et al. (2017b) have shown that the porosity evaluated on samples of Leitha limestone varies from 18% to 31% from a facies to another. For Mount Gambier limestone, Chen et al. (2020) have identified a porosity heterogeneity greater than 20% inside a single sample of only 2.5 cm in height.

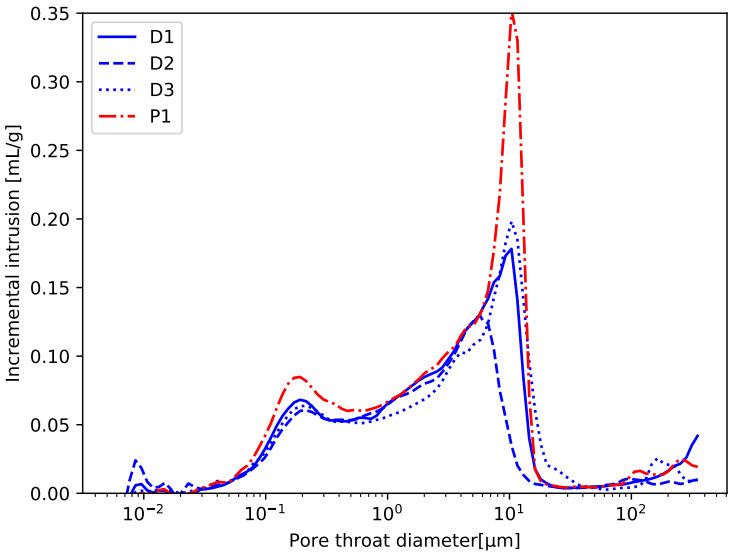

Figure 3: Pore throat diameter distribution from mercury intrusion porosimetry tests conducted on four specimens of SML in the initial state: P1 is cored from a high-porosity zone whereas D1, D2 and D3 are cored from denser zones. Mercury is injected up to a pressure of 227 MPa.

3 Experimental Equipments and Methods

Axisymmetric triaxial tests are performed on the cylindrical SML samples. Prior to loading, the sample is imaged by XRCT (initial state). Then, loading is applied in several stages. After each stage, the sample is unloaded and imaged with the same imaging parameters (ex-situ testing conditions). DVC analyses are performed thereafter on two consecutive images taken before and after a loading stage in order to compute local displacement fields at a spatial resolution associated with the used correlation window. Strain maps throughout the whole sample are then evaluated, using a FEM type differentiation of the displacement maps, at a local gauge length similar to the correlation window size. Strain localization bands may subsequently be identified. A method is developed to characterize the type of the bands based on kinematic considerations. In addition, a method to compute local porosity maps defined at a similar scale from XRCT images is developed. These maps will be superimposed with the computed strain maps in section 4.

3.1 Triaxial Testing

Triaxial tests are performed at a controlled temperature of 25°C. To avoid water effect on SML strength as reported by Baud et al. (2017a), samples are dried at 60°C for 48 hours and all the tests are performed in dry conditions. Macroscopic strains are measured by means of 6 Linear Variable Differential Transformers (LVDT): two along the axial direction and four along the radial one. The radial LVDTs are put at the mid-height of the sample along two orthogonal directions and the axial strain is measured over a height of 5 cm. A constant axial strain rate of 10^{-5}/sec is applied during the experiments by controlling the piston displacement. Circular pieces of teflon with a thickness of 1 mm are disposed at the interfaces between the sample and the loading stainless steel pistons, where grease is added in order to reduce friction boundary effects and to allow slippage at the top and the bottom of the sample.

3.2 X-Ray Computed Tomography

The unloaded samples are imaged in the initial configuration before the test and after each loading stage, using an UltraTom microtomograph (RX-Solutions, Chavanod, France), equipped with a 230kV microfocus Hama-

matsu L10801 X-Ray generator associated with a PaxScan 2520V flat panel detector used at full resolution (Varian, Palo Alto, USA). A copper filter of 0.5 mm in thickness is placed in front of the beryllium window of the generator, in order to filter low energy radiations. This helps reducing the so-called beam-hardening artefact which would have occured since large samples are imaged and because calcite, the main mineral of the SML, is opaque to low energy X-Ray radiations. In order to improve the contrast of images, the main source parameters have been chosen as: an accelerating voltage of 100 kV and an electron beam intensity of 500 μA. The XRCT observations are conducted using the so-called "stack mode", as an image of the full sample is sought, with the best possible resolution: the sample rotates around itself, whereas the source and detector are translated vertically, step by step. At the beginning of a scan, the source is in front of the upper part of the sample. After a 360° rotation, the source and detector move downward and the process is repeated. Finally, the image is composed of 6 levels. For each level, 1440 mean projections are recorded, each one is obtained by averaging 18 radiographs at a fixed rotation angle (a projection corresponds to an increment of rotation of 0.25°). Averaging allows to reduce random image noise. The 3D images are reconstructed using a voxel size of $24 \times 24 \times 24$ μm^3 by means of the X-Act software (RX-Solutions, Chavanod, France), based on the standard filtered back projection algorithm for conical projection (Feldkamp et al., 1984). A cylindrical reference sample of the same material is systematically imaged together with all unloaded samples in the same imaging conditions. This sample, of 4 cm in diameter and height, is conserved in constant temperature and humidity conditions and is supposed to remain unmodified. Imaging of the reference sample is therefore useful to calibrate the images of consecutive observations and to evaluate the error of the correlation method.

3.3 Digital Volume Correlation

The DVC analysis is performed on the images using the in-house developed software CMV3D (Bornert et al., 2004; Lenoir et al., 2007), with recent extensions of Gaye (2015). A regular 3D mesh of points, with a spacing of 40 voxels (= 0.96 mm), is defined inside the image recorded at the initial state. A correlation domain, whose size is chosen identical to the mesh size, is considered around each point, and the corresponding position of its center in the images of the deformed sample is found by minimizing the *zero centered*

normalized cross-correlation coefficient. An interpolation is done to locate the points that do not have a sufficient correlation coefficient. It consists in fitting a uniform gradient of transformation using the positions and motions of the 15 nearest found points (for details, see Gaye (2015)).

The deformation field is computed using 8-node trilinear finite elements defined in such a way that their nodes coincide with the correlation domains centers. This operation and the evaluation of the linearized strain tensor are averaged over each element by means of the Paraview software, using the "compute derivative" filter (Ayachit, 2015). Once the incremental strain tensor of an element $\underline{\underline{\epsilon}}$ is calculated, the volumetric deformation defined as the trace ($\epsilon_v = \mathrm{Tr}(\underline{\underline{\epsilon}})$) can be assessed (one increment corresponds to one loading stage). In addition, it is possible to evaluate the shear strain magnitude ($\gamma = \sqrt{2\underline{\underline{e}} : \underline{\underline{e}}}$) where $\underline{\underline{e}}$ is the deviatoric strain tensor $\underline{\underline{e}} = \underline{\underline{\epsilon}} - \frac{1}{3}\mathrm{Tr}(\underline{\underline{\epsilon}})\underline{\underline{I}}$ and $\underline{\underline{I}}$ is the identity matrix. Note that the DVC is applied on the reference sample in order to evaluate the strain field uncertainties and to correct for magnification variations, whenever present. The order of magnitude of the error in the local strain quantities evaluation is about 10^{-3} as 90% of the volumetric strain components in the undeformed reference sample range between -1.35 $\times$ 10^{-3} and 1.35 $\times$ 10^{-3} (see A for details). It is worthwhile to mention that the minimum thickness of a deformation band that can be measured on such maps is limited to the size of one element, i.e. 0.96 mm in our case.

3.4 Deformation Bands Type

Following the definition of Hill (1962), deformation bands are thin layers bounded by two parallel material discontinuity surfaces of the incremental strain tensor. Depending on the kinematics of strain localization, five categories of deformation band can be distinguished: pure compaction band, pure dilation band, pure shear band, compactive shear band and dilatant shear band (Rudnicki and Rice, 1975).

Intense deformation occurs inside a strain localization band, whereas much lower deformation takes place outside the band (in the order of the measurement error, e.g. see Figure 4). Thus, the discontinuity of the strain tensor across the band $[[\underline{\underline{\epsilon}}]]$ can be approximated by neglecting the strain outside the band $[[\underline{\underline{\epsilon}}]] = \underline{\underline{\epsilon}}^b - \underline{\underline{\epsilon}}^o \simeq \underline{\underline{\epsilon}}^b$, where $\underline{\underline{\epsilon}}^b$ and $\underline{\underline{\epsilon}}^o$ represent the strain tensors inside and outside a band respectively. The procedure to characterize a band consists in defining manually a tangent plane to a deformation band detected on a strain map as shown in Figure 4. This plane is chosen at the middle of

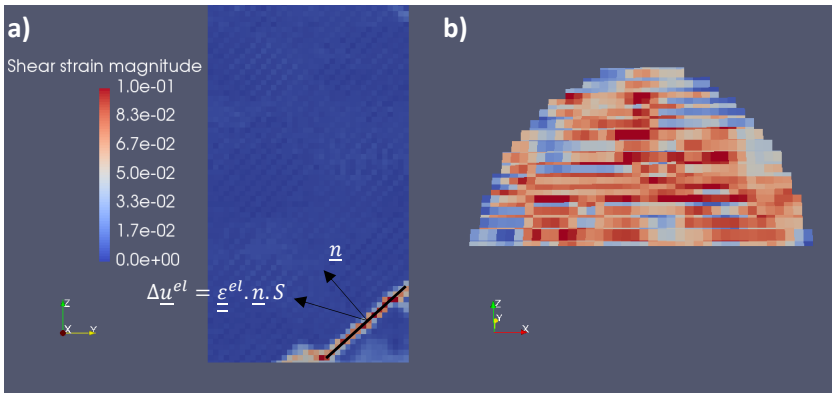

Figure 4: **(a)** Definition of the plane of a strain localization band. The displacement vector for each element along the black solid line is evaluated, where S is the element size; **(b)** Cross-section through the DVC strain map along the plane of the band.

the band and a unique unit outward normal vector $\underline{n}$ is thus defined along the band. Then, the strain tensor of each element inside the band permits to calculate the relative displacement vector $\Delta\underline{u}^{\text{element}} = \underline{\underline{\epsilon}}^{\text{element}}.\underline{n}.S$, where S is the length of the segment of direction $\underline{n}$ across the element. The Normalized Scalar Product (NSP) of the outward unit normal vector $\underline{n}$ and the relative displacement vector $\Delta\underline{u}^{\text{element}}$ for an element inside the band is calculated as:

$$NSP^{\text{element}} = \frac{\underline{n} \cdot \Delta\underline{u}^{\text{element}}}{\|\Delta\underline{u}^{\text{element}}\|} = \frac{\underline{n}.\underline{\underline{\epsilon}}^{\text{element}}.\underline{n}}{\|\underline{\underline{\epsilon}}^{\text{element}}.\underline{n}\|} \tag{1}$$

It is noted that the value is independent on S, but solely depends on the strain in the element within the band and the overall orientation of the band. The NSP^{element} is thereafter calculated for each element through which the central line of the band passes. Finally, the normalized scalar product of the band NSP^{band} is evaluated as the mean value over all the considered elements $NSP^{\text{band}} = \langle NSP^{\text{element}} \rangle_{\text{band}}$, allowing to define the band type as summarized in Table 2. Pure compaction and dilation bands are identified for $NSP^{\text{band}} = -1$ and $NSP^{\text{band}} = +1$ respectively. In case of orthogonal vectors ($NSP^{\text{band}} = 0$), a pure shear band is identified. Compactive and dilatant shear bands are intermediate categories for which $-1 < NSP^{\text{band}} < 0$ and $0 < NSP^{\text{band}} < 1$ respectively.

Table 2: Band types depending on the normalized scalar product value.

Band type	Pure compaction band	Compactive shear band	Pure shear band	Dilatant shear band	Pure dilation band
NSP	-1	$-1 < .. < 0$	0	$0 < .. < 1$	1

3.5 Porosity Maps

From XRCT observations, one can obtain 3D images of the microstructure at successive states of deformation. These images show a heterogeneity of porosity. Thus, it is interesting to build 3D local porosity maps and compare them with the 3D deformation maps provided from DVC.

3.5.1 Subvolume Size

Porosity is a non-local quantity since it cannot be evaluated at a material point, but is defined over a subvolume of finite size. In this study, the subvolume is assumed to have a spherical shape of radius R in order to quantitatively reflect the fluctuations of porosity at the centimetric scale. The size of this subvolume over which the porosity is computed should be sufficiently larger than the characteristic pore and grain sizes (about 0.3 mm, see Figure 2) and sufficiently smaller that the characteristic size of the porosity heterogeneity (around 1 cm). Finally, a diameter of 0.96 mm, corresponding to the size of the finite element over which the strain tensor is computed (see Section 3.3), is chosen as the appropriate diameter for porosity evaluation. Local strain and local porosity are thus evaluated at the same scale which makes sense in view of seeking the link between the observed heterogeneities of both quantities.

3.5.2 Porosity Computation

Since three different phases (pores, quartz grains, and calcite grains) are present in SML, the average grey value calculated over a random volume $\langle g \rangle$ can be written as:

$$\langle g \rangle = \phi . g_{\text{pore}} + f_{\text{quartz}} . g_{\text{quartz}} + f_{\text{calcite}} . g_{\text{calcite}} \tag{2}$$

where ϕ is the porosity, f_{quartz} and f_{calcite} are the volume fractions of quartz and calcite minerals respectively (with $\phi + f_{\text{quartz}} + f_{\text{calcite}} = 1$). Since the solid

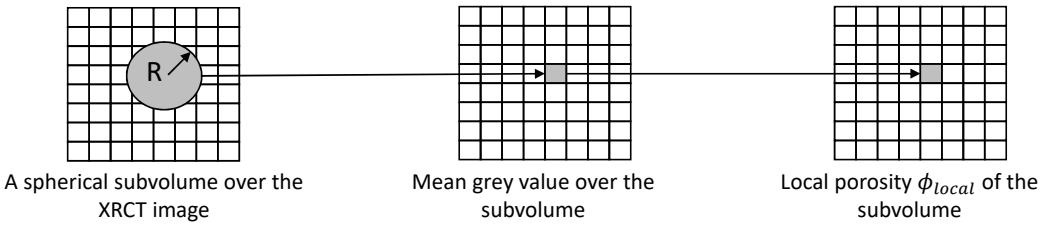

Figure 5: From XRCT images to porosity maps: Local porosity evaluation over a subvolume of radius R.

matrix is formed by calcite and quartz, two minerals which have very close linear absorption coefficients over the range of energy of the X-Ray used to scan the samples, the following assumption is made: $g_{\text{quartz}} \simeq g_{\text{calcite}} \simeq g_{\text{solid phase}}$ (for details on the justification of this approximation, see B). Consequently, Equation 2 can be written as follows:

$$\langle g \rangle = \phi . g_{\text{pore}} + (1 - \phi) . g_{\text{solid phase}} \tag{3}$$

Equation 3 is applied at two levels: first, for the whole sample, then on each subvolume of radius R. For a given sample of known global porosity ϕ, the quantities $\langle g \rangle$ and g_{pore} are easily measured with the open-source software FIJI (Schindelin et al., 2012). Consequently, the grey level of the homogenized solid phase $g_{\text{solid phase}}$ can be calculated. Then, over each voxel of an XRCT image, a spherical subvolume of radius R is defined (Figure 5). This pseudo-sphere is composed of discrete voxels, the center of which have a distance smaller than R with respect to the sphere center. FIJI can smooth the images and give a mean value $\langle g \rangle_{sub}$ of the grey levels of all voxels inside the subvolume. Finally, the computation of each subvolume local porosity is straightforward. Figure 5 illustrates the steps of a porosity map computation. Paraview is then used to visualize the porosity maps.

4 Experimental Results

The convention of negative values for a compactive behavior is adopted in this study. The mean stress is defined as $p = \frac{\text{Tr}\,(\underline{\underline{\sigma}})}{3}$ whereas the shear stress intensity is defined as the square root of the second invariant of the deviatoric part ($\underline{\underline{s}} = \underline{\underline{\sigma}} - p\underline{\underline{I}}$) of the stress tensor: $q = \sqrt{\frac{1}{2}\underline{\underline{s}} : \underline{\underline{s}}}$. Let σ_1 and σ_3 denote the minimum and maximum principal stresses respectively. In axisymmetric

triaxial compression, the stress state is diagonal with $\sigma_1 < \sigma_2 = \sigma_3 < 0$. Therefore, the mean stress and the shear stress intensity are expressed as: $p = \frac{\sigma_1+2\sigma_3}{3}$ and $q = \frac{\sigma_3-\sigma_1}{\sqrt{3}}$.

4.1 Preliminary Tests

Figures 6a, b show typical stress-strain curves for samples tested under axisymmetric triaxial loading. ϵ_a is the axial strain and ϵ_v is the volumetric strain. Following the definition of Wong et al. (1997), plasticity onset is detected on the p vs ϵ_v plot and is denoted by P^* and C^* in hydrostatic and deviatoric loading respectively. Under hydrostatic loading, the SML sample seems to deform homogeneously, as no barrel-shaped mode is obtained after more than 6% of compressive volumetric strain. The yield stress P^* is evaluated at -14.5 MPa. Deviatoric loading causes an earlier compaction ($P^* < C^* < 0$). At low confining pressure ($\sigma_3 = -1$ MPa), a peak stress is observed (Figure 6b), followed by a softening regime. After around 2% of axial strain, it is observed that two conjugate shear bands are formed as shown in Figure 7. At relatively high confining pressures ($\sigma_3 = -11$ MPa), an overall hardening regime is observed after the elastic limit. Beyond 4% axial strain, one may visually detect the formation of deformation bands (Figure 7). Due to the high porosity of SML, no dilatancy is measured by the LVDTs, even at low confining pressure. The transitional regime occurs at $\sigma_3 = -6$ MPa and is characterized by a perfectly plastic response. A visual inspection of the sample surface after deformation reveals some signs of strain localization, similar to the sample tested at high confining pressure. To complete the characterization of the yield surface, two additional uniaxial tests are performed (Figure 6c). The uniaxial compressive strength is obtained at around 10 MPa. Moreover, the tensile strength σ_t is evaluated at 1.2 MPa by means of two Brazilian tests. Finally, all the data are gathered and yield stresses of SML are plotted in Figure 6d. The results are consistent with those of Baud et al. (2009) and Baud et al. (2017a). Four different loading conditions are thus selected for a detailed study of the local strain heterogeneities by means of XRCT and DVC. Each subsection below is devoted to one of these loading cases:

1. Hydrostatic loading test.

2. High confining pressure test (11 MPa).

3. Low confining pressure test (1 MPa).

4. Intermediate confining pressure test (6 MPa).

The yield stresses corresponding to these samples are represented with solid triangles in Figure 6d. Since X-Ray imaging is done ex-situ, samples must be unloaded after each loading stage, then extracted from the triaxial machine to be imaged. Thereafter, they are put back inside the triaxial cell where further loading is applied. Thus the deformation tensor which is computed from the XRCT images corresponds to the irreversible (plastic) part of the total deformation (Figure 8).

4.2 Hydrostatic Loading

A SML sample, with an overall porosity of 38.2%, is tested under hydrostatic loading conditions (Figure 8a). The sample is imaged by XRCT three times: in the initial state and after each loading stage, and DVC is thus applied twice (once for each loading stage). In the first stage, loading is stopped right after the critical hydrostatic pressure $P^* = 15.9$ MPa. The computed volumetric strain map shows the onset of a plastic deformation at the bottom part of the sample (Figure 9a). The compactive strain evaluated inside this zone is around 2%, whereas the remaining zones of the sample are almost undeformed. During the second loading stage, a linear overall hardening is obtained (Figure 8a) and a residual overall volumetric strain of 5.5% is measured. The incremental volumetric strain map shows that a heterogeneous but diffuse compaction occurs in the sample, without any sign of deformation bands (Figure 9a). Inside the compacted zones, the volumetric strain can go up to 10%. However, many zones are observed to remain undeformed (more precisely, the measured local strain is of the order of the DVC uncertainty: 0.1%).

The DVC strain maps are compared with the porosity maps (Figure 10). Three zones can be distinguished: high-porosity zones (illustrated by arrows A) where the porosity is higher than 40%, low-porosity zones (arrow B) where the porosity is lower than 35% and the interface zones (arrow C). A pure compaction without any shear evidence is observed inside zones A, whereas zones B form stiff inclusions and remain essentially undeformed. Moreover, a significant shear strain takes place in zones C due to the stiffness contrast between zones A and B, as the stress at the local scale may not be homogeneous. The incremental plastic shear strain intensity can go up to 10%

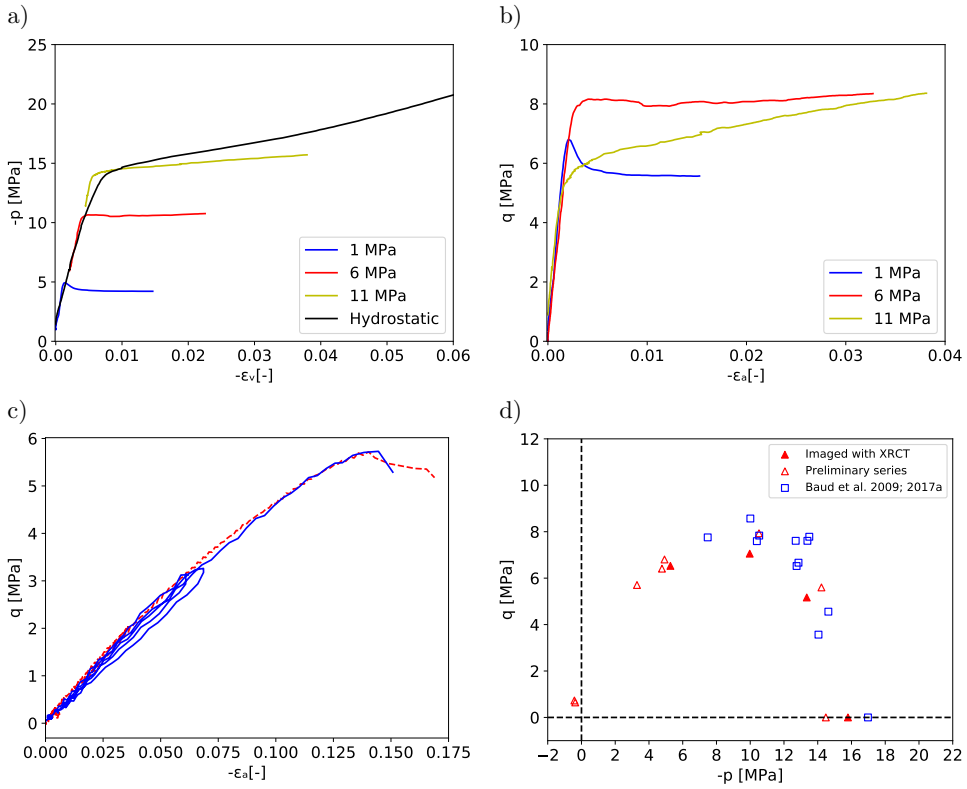

Figure 6: Mechanical reponse of the SML tested under several confining pressures: **(a)** Mean pressure vs volumetric deformation; **(b)** Shear stress intensity vs axial strain; **(c)** Two uniaxial tests; **(d)** Yield stresses: empty red triangles for the preliminary tests, solid red triangles for the samples studied later with XRCT & blue squares for data from Baud et al. (2009) and Baud et al. (2017a).

Figure 7: Left: Conjugate shear bands observed at low confining pressure $\sigma_3 = -1$MPa; Right: Deformation bands observed at high confining pressure $\sigma_3 = -11$MPa.

Table 3: Mean values of volumetric and shear strain magnitudes of the three domains selected in Figure 10a during the second loading stage.

Zone	Mean shear strain magnitude [%]	Mean volumetric strain [%]
A	1.6	-6.8
B	0.9	-0.8
C	5.1	-6.9

in these zones. It is observed that higher porosity contrasts promote higher shear strains (see the interface zone on the bottom left part of the sample in Figure 10). Nevertheless, volumetric compaction is also observed inside zones C, in the same range of the shearing intensity (10%). For instance, three domains are selected on Figure 10a and the mean values of volumetric and shear strain magnitudes are presented in Table 3.

A SEM observation of the thin section extracted from this sample is presented in Figure 11a, where the contrast between deformed high-porosity zones and undeformed low-porosity zones is shown. The large and cemented calcite grains are observed to remain undeformed in the latter zones, whereas pervasive calcite grain crushing occurs in high-porosity zones. Indeed, the observations performed on high-porosity zones of the SML in the initial state do not show the presence of such amounts of small grains surrounded by pow-

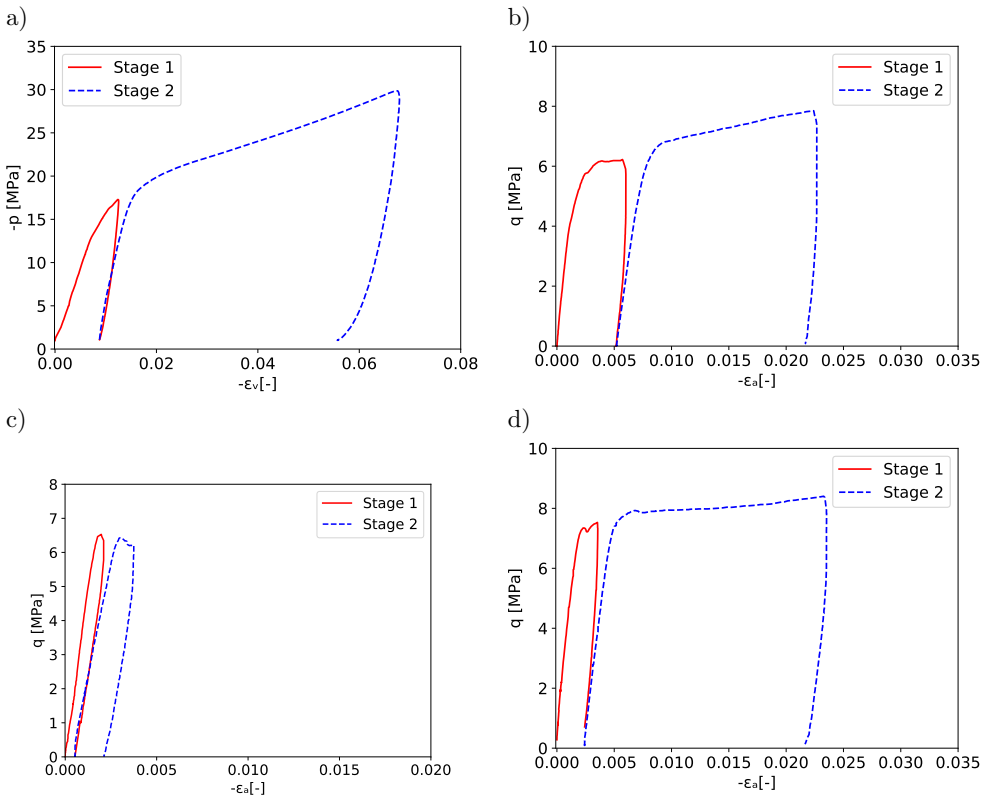

Figure 8: Loading stages applied on the SML samples tested under: **(a)** Hydrostatic loading; Triaxial loading **(b)** $\sigma_3 = -10.5$ MPa; **(c)** $\sigma_3 = -1.5$ MPa; **(d)** $\sigma_3 = -6.0$ MPa.

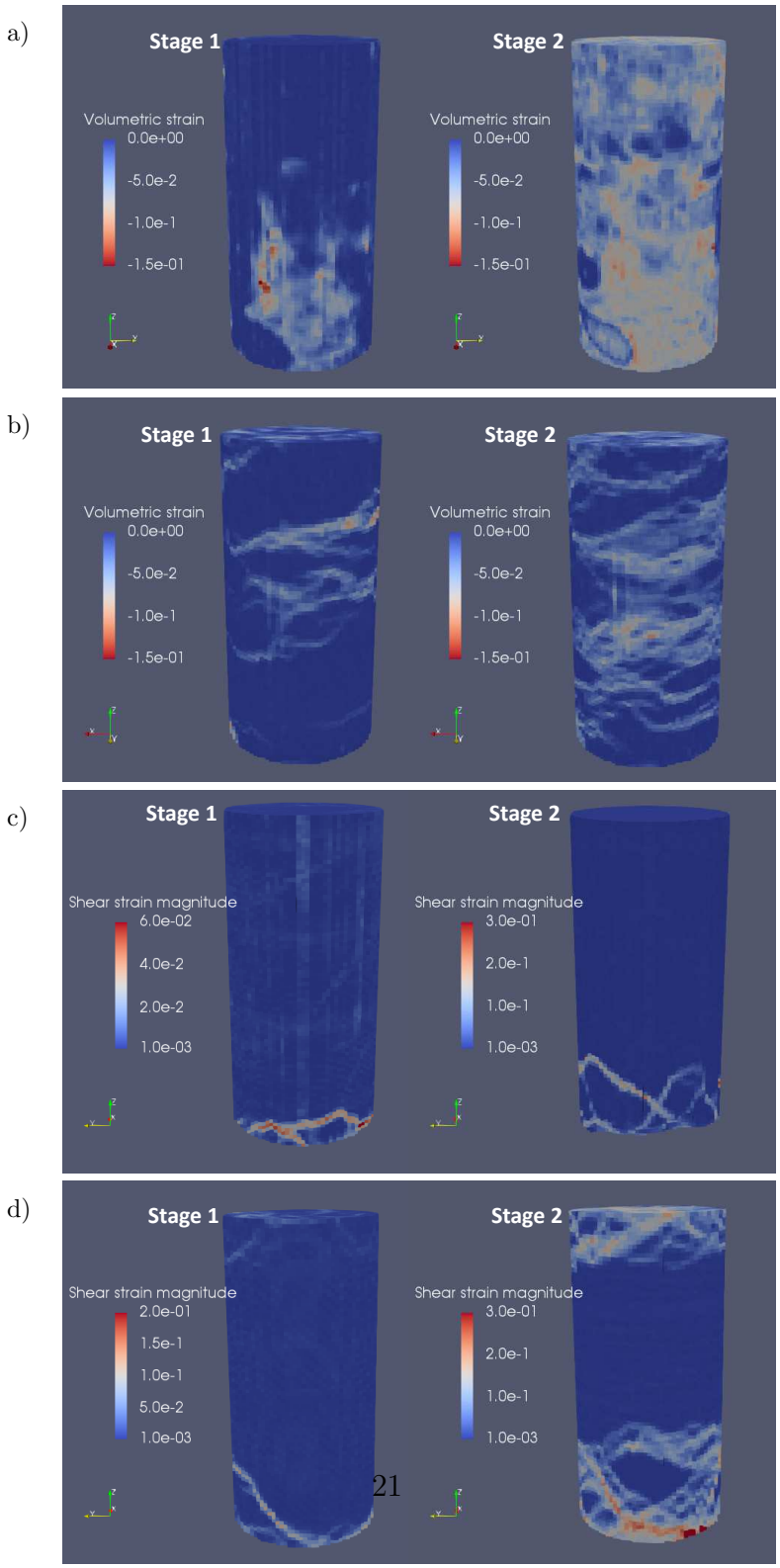

Figure 9: Incremental volumetric strain or shear strain magnitude maps computed for the samples tested under: **(a)** hydrostatic loading; **(b)** $\sigma_3 = -10.5$ MPa; **(c)** $\sigma_3 = -1.5$ MPa; **(d)** $\sigma_3 = -6.0$ MPa. One increment

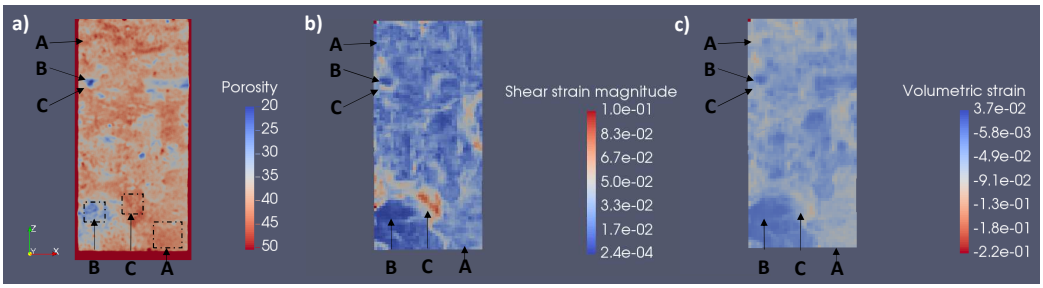

Figure 10: Vertical cross-sections of the sample tested under hydrostatic loading during the second loading stage: **(a)** Porosity map before loading; **(b)** Shear strain magnitude map; **(c)** Volumetric strain map.

ders (see Figure 2). In addition, quartz grains appear to remain undeformed as opposed to calcite grains in accordance with Baud et al. (2017a) observations. As a consequence of grain crushing, powders are formed and pores are subsequently filled. On the other hand, it is observed that large pores inside the denser zones (with sizes up to 1 mm) do not collapse (Figure 12). According to the experimental observations of Vajdova et al. (2010); Ji et al. (2012) on several limestones, larger pores are weaker and may collapse prior to smaller ones. This is not observed for the SML, since these large pores are protected by the surrounding rigid matrix of cemented grains.

4.3 Triaxial Test under High Confining Pressure

Another SML sample, with an overall porosity of 37.7%, is tested in axisymmetric triaxial loading under a relatively high confining pressure of 10.5 MPa (Figure 8b). Again, the sample is imaged by XRCT three times. The first loading stage is stopped just after the plasticity onset ($C^* = 13.35$ MPa) and the residual axial strain measured by the LVDTs is 0.5%. Several strain localization bands are observed on the computed strain maps (Figure 9b). A vertical cross-section shows that these quasi planar bands have high-angle inclination with respect to the minimum principal stress direction (Figure 13a). Their thicknesses vary from 1 to 3 mm (1 to 3 elements). In addition, boundary effects are observed at both ends of the sample, as conjugate shear bands are formed at the upper part, but are less developed at the bottom. The compaction evaluated inside these bands can reach 6%, whereas the deformation is very low outside. In the second stage, an overall hardening is

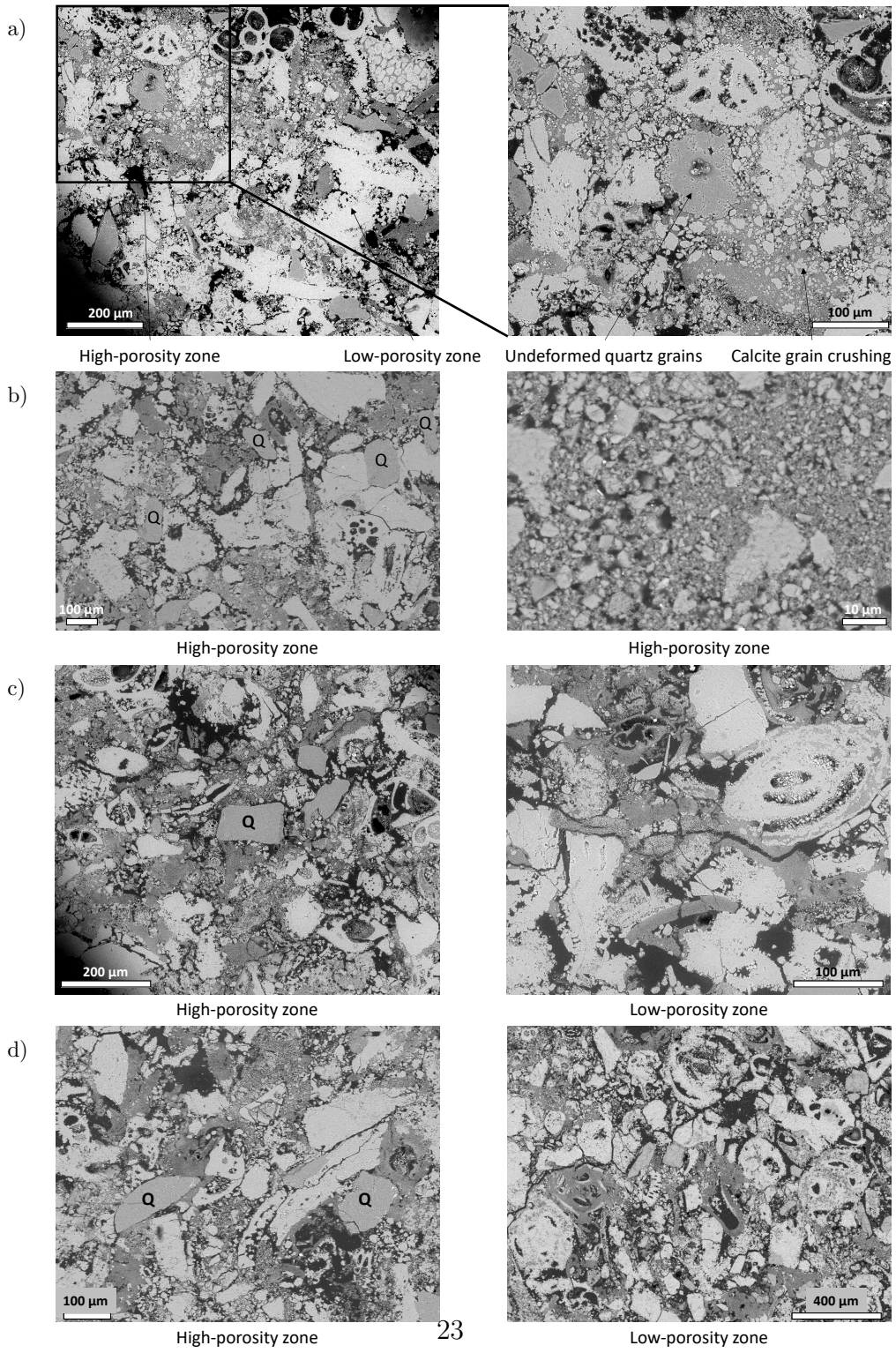

Figure 11: SEM observations of thin sections prepared after the second loading stage from the SML samples tested under: **(a)** hydrostatic loading; **(b)** $\sigma_3 = -10.5$ MPa; **(c)** $\sigma_3 = -1.5$ MPa; **(d)** $\sigma_3 = -6.0$ MPa. Q denotes quartz grains.

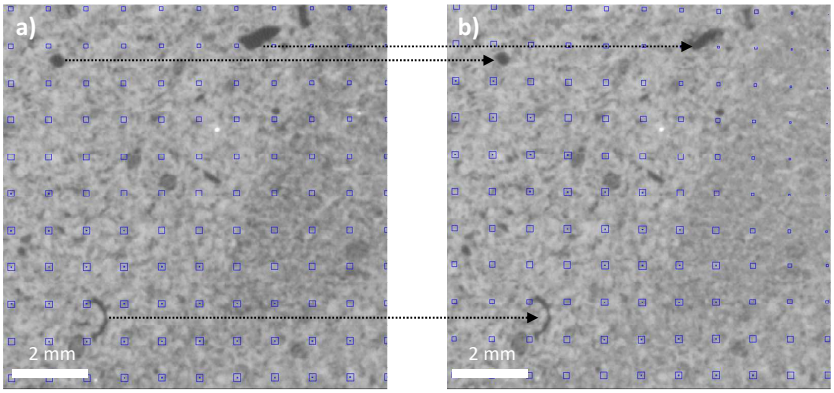

Figure 12: Undeformed large pores identified in the low-porosity zones in the sample tested under hydrostatic loading **(a)** before and **(b)** after the second loading stage.

observed and a residual axial strain of 2.15% is measured. In this stage, strain continues to localize inside the previously formed bands (Figures 9b and 13a). In addition, the deformation bands become thicker while applying further loading. Several new bands are detected, which coalesce together and form thicker zones of compaction. At the borders, highly damaged zones are observed where diffuse compaction occurs due to a possible boundary effect. The increment of compactive volumetric strain evaluated inside the deformation bands can reach 7%.

Deformation bands are observed to lay inside high-porosity zones, whereas denser zones seem to remain undeformed (Figure 14). The strain localization bands pattern would thus be controlled by porosity fluctuations at the scale of one centimeter. The different orientations of the bands inside the same sample are likely to be linked to the heterogeneity of the porosity. When it propagates, a band would avoid denser zones and follow a path inside more porous ones, where densification takes place.

Similarly to the sample tested under hydrostatic loading, pervasive calcite grain crushing occurs in high-porosity zones, as shown by the SEM images on the thin section (Figure 11b). Again, quartz grains (denoted by the letter Q) remain undamaged in these zones. Moreover, many large pores in the low-porosity zones are protected by the surrounding material as they remain undeformed after strain localization (Figure 15).

In order to characterize the deformation band types, several ones are

a)

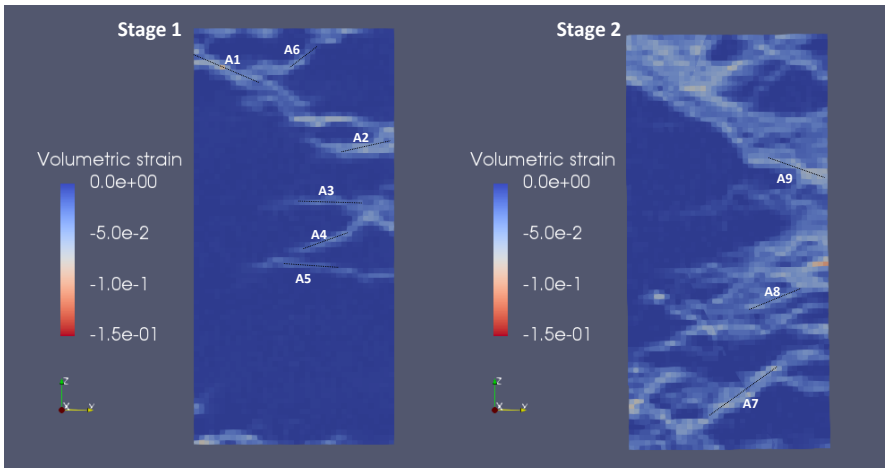

b)

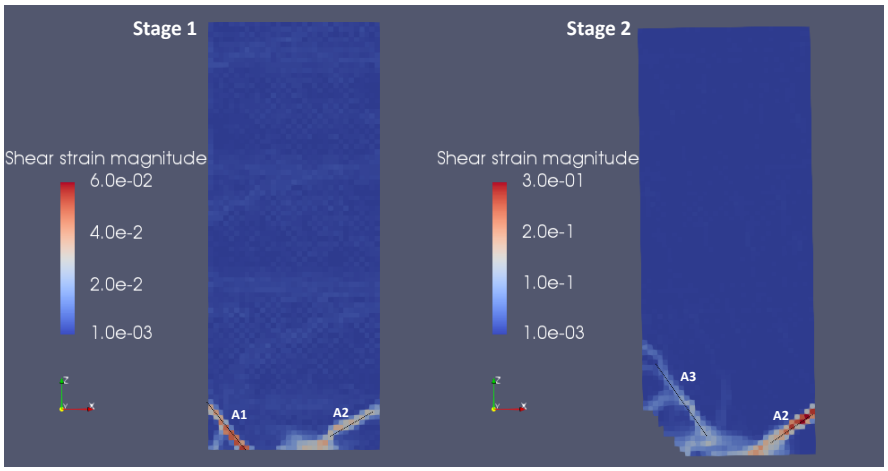

c)

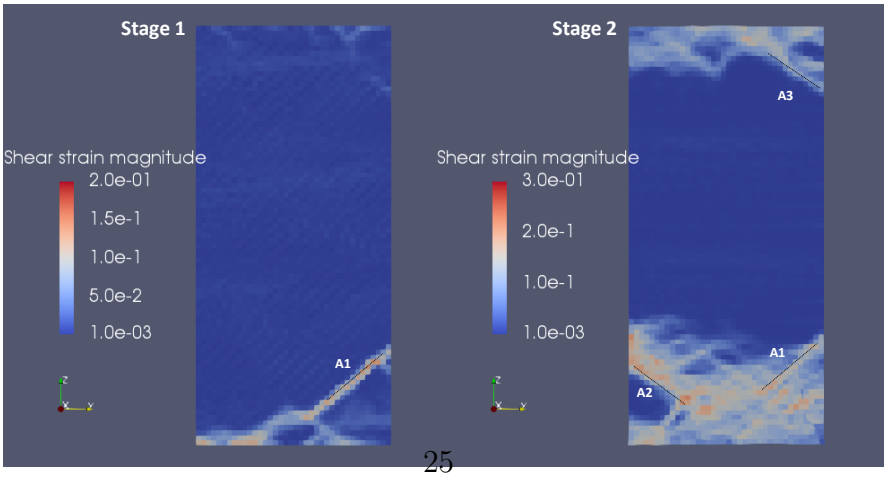

Figure 13: Strain localization bands selection on vertical cross-sections of the computed strain maps in both loading stages: **(a)** $\sigma_3 = -10.5$ MPa; **(b)** $\sigma_3 = -1.5$ MPa; **(c)** $\sigma_3 = -6.0$ MPa.

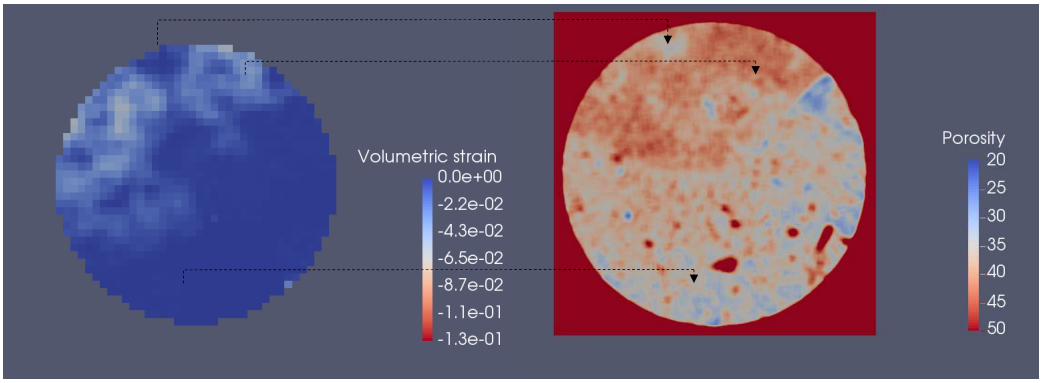

Figure 14: SML sample tested under high confining pressure: a typical transverse cross-section showing that strain is localized inside high-porosity zones.

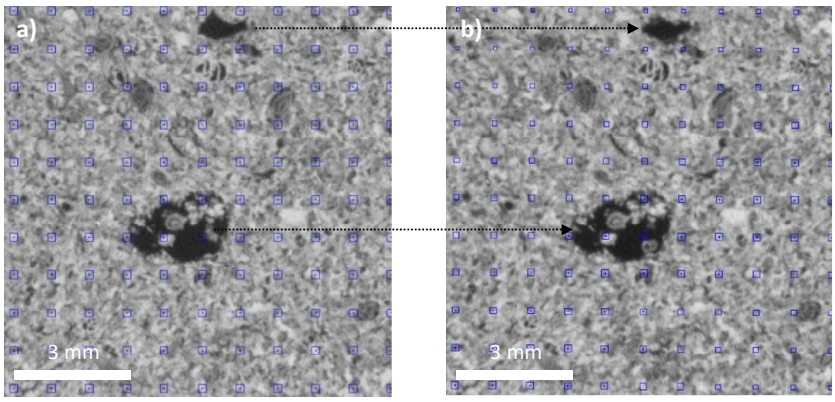

Figure 15: SML sample tested under high confining pressure: Large pores inside low-porosity zones remain undeformed: XRCT image **(a)** at the initial state; **(b)** after the second loading stage.

Table 4: Band types, orientations (θ) and thicknesses in the sample tested at high confining pressure (10.5 MPa). θ is the angle between the axis of the sample and the deformation bands.

	Band	NSP^{band}	θ°	Thickness [mm]	Type
After Stage 1 of loading	A1	-0.91	69.9	2-3	Compaction band
	A2	-0.91	80.5	2	Compaction band
	A3	-0.97	84.1	1	Compaction band
	A4	-0.94	68.2	1-2	Compaction band
	A5	-0.94	83.2	1	Compaction band
	A6	-0.82	48.2	1-2	Compactive shear band
After Stage 2 of loading	A7	-0.84	56.3	3-4	Compactive shear band
	A8	-0.98	71.6	2	Compaction band
	A9	-0.94	63.4	2-3	Compaction band

selected on the DVC maps. The selected bands in the first and second loading stages are denoted by A1 to A6, and A7 to A9 respectively (Figure 13a). The values of the *NSP* (see Section 3.4) are given in Table 4, together with the band orientations and thicknesses. Except for band A6, the *NSP* values ranges between -1 and -0.9 indicating that they are of pure compaction type. Their angles with respect to the axial direction are higher than 70°. In contrast, the conical shape, the low angle and the value of *NSP* (-0.82) suggest that A6 is a compactive shear band, induced by boundary effects. As for the second stage, the bands A8 and A9 are high-angle bands ($\theta > 63^{\circ}$) with low *NSP* values (< -0.9). They are thus identified as pure compaction bands. On the other hand, the band A7, which has an orientation of 56.3°and a value of $NSP > -0.9$ is identified as a compative shear band. In summary, following the classification presented in Table 4, a pure compaction band is defined when $NSP < -0.9$ and $\theta > 63^{\circ}$. These bands appear in the central part of the sample, whereas compactive shear bands, having a conical shape near the borders, are induced by boundary effects.

4.4 Triaxial Test under Low Confining Pressure

A SML sample, having an overall porosity of 37.9%, is tested under a relatively low confining pressure of 1.5 MPa (Figure 8c). In the first stage, loading is stopped at the peak stress (axial stress of 12.8 MPa corresponding to a shear stress intensity $q = 6.5$ MPa). The peak stress occurs when

two conjugate strain localization bands develop at the bottom of the sample (Figures 9c and 13b). The two bands, with a thickness of around 2 mm, are quasi perpendicular and have orientations of 52.4° and 43.2° with respect to the axial direction respectively. The local shear strain magnitude inside the bands reaches 6%. In the second stage, a slight softening occurs and a residual axial strain of 0.2% is measured. It is however worthwhile to remind that axial LVDTs cover only 5 cm of height and are disposed around the central zone of the sample, while the shear bands are formed near the boundaries so that the LVDT measurements are not representative of the global deformation of the sample. The DVC maps show that shear strain continues to increase in the previously formed band (denoted by A2 in Figure 13b), with no significant change of the band thickness (2 mm). New bands are detected, with thicknesses varying between 1 and 2 mm. The incremental shear strain magnitude inside the bands can go up to 30%. A highly damaged zone is also observed near the bottom boundary, suggesting that stress concentration induced by boundary effects may have triggered the strain localization bands.

The volumetric strain maps show a complex kinematic behavior inside the bands. When compared with the shear strain magnitude map, compaction and dilation are found to alternate along a single band (Figure 16). In contrast to the observations of the two previous loading cases, deformation bands at low confining pressure are observed to cross both high- and low-porosity zones. Dilation is mostly observed to occur in low-porosity zones where many cracks are induced by shearing (Figure 16d), while compactive volumetric strain is observed in more porous zones. The elements of the cross-section shown in Figure 16 having high levels of deformation ($|\epsilon_v| > 1.5\%$) are considered in Figure 17, where the volumetric strain is plotted against the porosity evaluated before loading. This plot clearly shows that compactive behavior takes place in zones with porosities greater than a threshold of about 41%, whereas shear bands crossing zones with porosities lower than this threshold undergo a dilatant behavior.

Figure 11c shows the comparison between typical SEM images of a high- and low-porosity zone crossed by a deformation band. A pervasive calcite grain crushing is observed in the former zone, and powders are formed. These fine particles are responsible for a pore filling mechanism and therefore, a reduction in the pore space. On the other hand, cracks are formed inside the intergranular cementation in low-porosity zones. Since no cracks were observed in the two previous loading cases, we could admit that these cracks

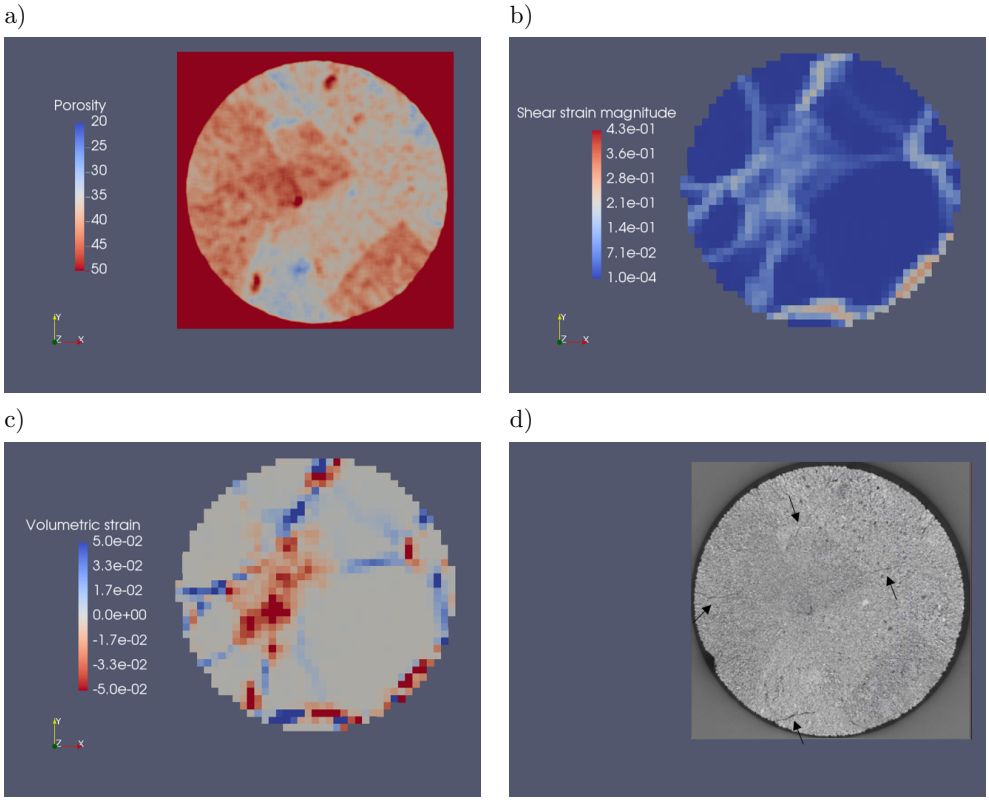

Figure 16: Transverse cross-sections through the maps of the SML sample tested under low confining pressure during the second loading stage: **(a)** Porosity map before loading; **(b)** Shear strain magnitude map; **(c)** Volumetric strain map; **(d)** XRCT image recorded after loading. The black arrows indicate new opened cracks.

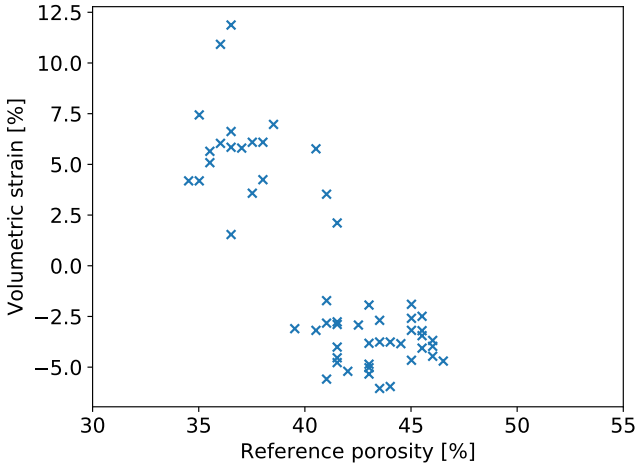

Figure 17: Plot of the incremental volumetric strains evaluated for several elements in the cross-section shown in Figure 16 with respect to their corresponding porosity values evaluated before loading. For the sake of clarity, only the elements having a volumetric strain larger than 1.5% in absolute value are shown.

most probably formed in due course of loading and are not unloading features. These cracks, which induce local dilatancy in the deformation band, propagate inside this "weaker material" and usually avoid to cross the dense grains as observed by Dautriat et al. (2011).

Two deformation bands are selected after the first loading stage and are denoted by A1 and A2 (Figure 13b). The *NSP* of the band A1 is evaluated at 0.07 (Table 5), which is thus identified, on average, as a pure shear band. However, local compaction and dilation are identified inside this band. Indeed, the *NSP* values of the elements along the central line vary between -0.3 and 0.3. Therefore, the band changes locally its type from dilatant shear band to compactive shear band depending on whether it crosses a low- or high-porosity zone. As for the band A2, the compactive behavior is more dominant and the calculated *NSP* for the elements are more homogeneous. The corresponding *NSP* is evaluated at -0.17 and the band A2 is therefore identified as a compactive shear band. In the second stage of loading, it is observed that the *NSP*, the orientation and the thickness of band A2 do not vary significantly. No further observation was possible for band A1 because

Table 5: Band types, orientations (θ) and thicknesses in the sample tested at low confining pressure (1.5 MPa). θ is the angle between the axis of the sample and the deformation bands.

	Band	NSP^{band}	θ°	Thickness [mm]	Type
After Stage	A1	0.07	52.4	2	Pure shear band
1 of loading	A2	-0.17	43.2	2	Compactive shear band
After Stage	A2	-0.19	46.0	2	Compactive shear band
2 of loading	A3	0.16	34.6	1-2	dilatant shear band

a small piece of the sample broke away before imaging. The band A2 is thus still identified as a compactive shear band. As for the band A3, dilation seems to be dominant, and the corresponding *NSP* is evaluated at 0.16. This band, with an orientation of 34.6° with respect to the sample axis, is identified as a dilatant shear band. However, similarly to the band A1 in the first loading stage, local compaction and dilation are observed to fluctuate inside the band A3: the *NSP* values of the elements vary between -0.2 and 0.5. It turns out that the band crosses mainly a low-porosity zone of porosity around 30%, which can explain why dilation is dominant in this case.

4.5 Triaxial Test under Intermediate Confining Pressure

A SML sample with an overall porosity of 38.0% is tested under an intermediate confining pressure of 6 MPa, which corresponds to the brittle-ductile transitional regime (Figure 8d). In the first stage, loading is stopped after the plasticity onset, evaluated at a shear stress intensity q=7.0 MPa (equivalent to 18.2 MPa of axial loading). The DVC strain maps make evidence of the formation of a deformation band in the lower part of the sample at the plasticity onset (Figures 9d and 13c). The band has an orientation of 50.2° with respect to the minimum principal stress direction, with a thickness between 2 and 3 mm (2 to 3 elements). The shear strain magnitude inside the band has a mean value around 10% and can go up to 14%. Shear strain caused by boundary effects are observed close to the bottom end of the sample and may have triggered the deformation band through the sample. On the upper part of the sample, the amount of strain is very low in comparison with the bottom part. Some traces of a deformation band begin to appear,

but a full strain localization band is not developed yet. In the second stage, a plateau is observed in the shear stress intensity versus LVDT measurement axial strain curve (Figure 8d), characterizing a perfectly plastic behavior. The shear stress intensity remains at 8 MPa, and a residual axial strain of 2.2% is measured. During this stage, shear strain continues to localize inside the previously formed band (denoted by A1). The thickness of the band does not evolve significantly. Despite the formation of a thick damaged zone near the bottom boundary, a new major deformation band can be observed (denoted by A2 in Figure 13c). Strain localization is mainly observed in high-porosity zones. Some boundary effects are also present near the upper boundary, where a small cone of localized deformation is identified. A short deformation band can anyway be selected and is denoted by A3. The thickness of this band is around 2 mm. The shear strain magnitude inside the deformation bands can reach 20 to 25%. As for the volumetric strain, local compaction of 6 to 10% are assessed inside the bands.

Similarly to the previous sample, the volumetric strain maps show a complex kinematic behavior inside the bands, where compaction and dilation are found to alternate (Figure 18). Again, the deformation bands cross both high- and low-porosity zones. Cracks are formed in the low-porosity zones, inducing a local dilation (Figure 18d). Furthermore, SEM observations make evidence of the similarity of the involved micromechanisms between this sample and the previous one (Figure 11d). A pervasive calcite grain crushing is observed in the high-porosity zones and intergranular cracks are formed in the low-porosity zones.

Table 6 gathers the data of the bands type, orientation and thickness. The unique band A1 that forms just after plasticity onset has an orientation of 50.2° and is identified as a compactive shear band ($NSP = -0.67$). During the second stage, the band A1 is still a compactive shear band, having a slightly higher amount of shear (the *NSP* increases to -0.62). The two other bands A2 and A3 are also identified as compactive shear bands. The average *NSP* of the bands ranges between -0.50 and -0.79. The values of the *NSP* along the elements of the bands are homogeneous, and dilatant behavior does not seem to have a significant impact on the nature of the bands. The band orientations vary between 48° and 60°. The average orientation of the bands with respect to the axial direction is globally higher than those of the SML sample tested at low confining pressure, but lower than those of the SML studied at high confining pressure.

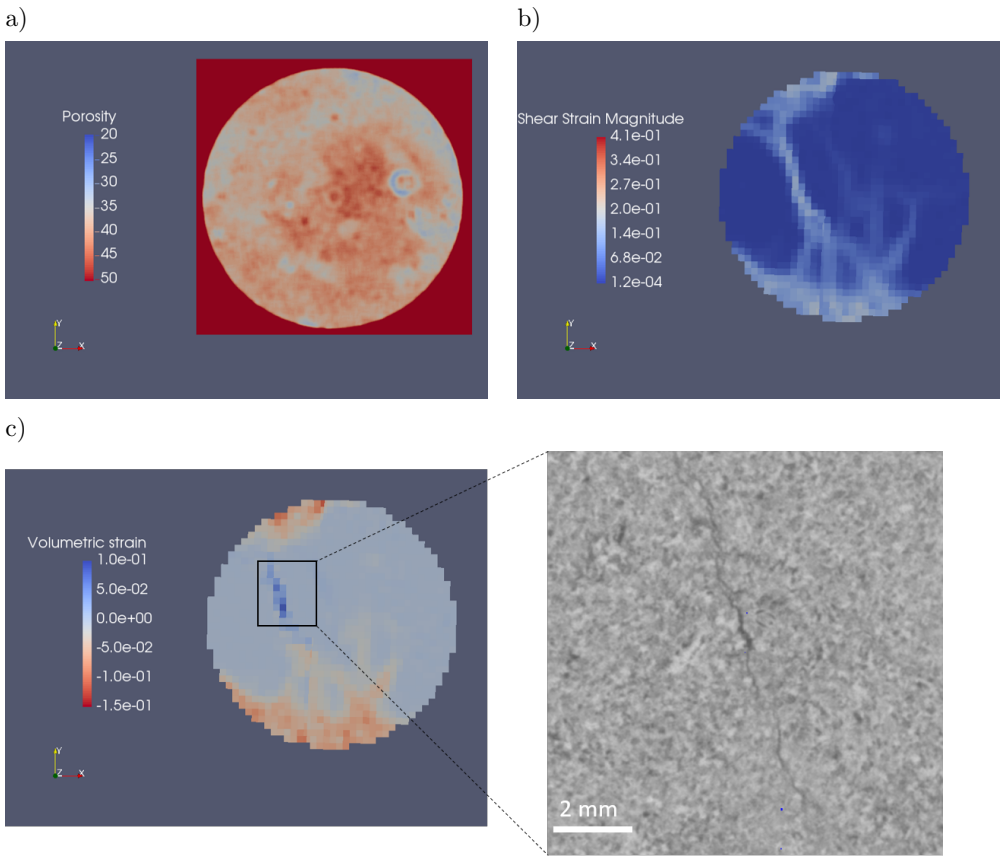

Figure 18: Transverse cross-sections performed on the maps of the SML sample tested under intermediate confining pressure during the second loading stage: **(a)** Porosity map before loading; **(b)** Shear strain magnitude map; **(c)** Volumetric strain map, with the corresponding XRCT cross-section recorded after loading.

Table 6: Band types, orientations (θ) and thicknesses in the sample tested at intermediate confining pressure (6 MPa). θ is the angle between the axis of the sample and the deformation bands.

	Band	NSP^{band}	θ°	Thickness [mm]	Type
After Stage 1 of loading	A1	-0.67	50.2	2-3	Compactive shear band
After Stage 2 of loading	A1	-0.62	50.2	2-3	Compactive shear band
	A2	-0.79	59.5	2-3	Compactive shear band
	A3	-0.50	47.7	2	Compactive shear band

5 Discussion and Conclusions

The mechanical behavior and the deformation modes of a high-porosity carbonate rock have been studied under several stress conditions. The DVC technique proves to be a relevant method for deformation bands identification in limestones. A simple post-processing method, that operates on the computed deformation maps in order to identify the band types, has been proposed. In addition, porosity maps have been computed and compared with deformation maps in order to understand the role played by the porosity heterogeneity in the deformation heterogeneity. The porosity field has been computed at a scale comparable to the local gauge length of the deformation maps.

Under hydrostatic loading, diffuse compaction is observed in high-porosity zones, whereas denser zones present stiff inclusions which remain undeformed. However, due to the stiffness contrast and strain incompatibilities, the stress field is heterogeneous in the material and intense shear strains are observed in the high-porosity zones close to the low-porosity ones. Calcite grain crushing is identified as the principal micromechanism of deformation in the high-porosity areas, in contrast to the quartz grains that almost remain undeformed. The fines produced by this process are observed in the pore space. At relatively high confining pressures, compaction bands are identified. These bands propagate in high-porosity zones, while denser zones remain mostly intact. Significant crushing of calcite grains is observed inside compaction bands. For low confining pressures, shear bands form at low-angle orientations with respect to the direction of minimum principal stress. The porosity heterogeneity does not play a significant role in the orientation and the path of shear bands, as the observed bands may cross both zones. However, it

affects the volumetric strain behavior: shearing a high-porosity zone induces a local compaction due to calcite grain crushing phenomenon. In contrast, shearing a low-porosity zone induces a local dilation due to intergranular cementation cracking. The brittle-ductile transitional regime is characterized by the formation of compactive shear bands. These bands propagate preferably through high-porosity zones similarly to compaction bands, with significant crushing of calcite grains. But in addition, they may also cross low-porosity zones, where cement microcracking can be observed similarly to shear bands.

The deformation bands orientations with respect to the minimum principal stress direction has a positive correlation with respect to the confining pressure. The porosity heterogeneity seems to play a secondary role in the bands orientation: compaction bands have orientations greater than 70°, shear bands have orientations lower than 50° and compactive shear bands have intermediate orientations.

The precautions considered at the boundaries have allowed to reduce boundary effects and prohibited the formation of compaction fronts growing toward the central part of the sample (e.g. as observed by Papazoglou et al. (2017)). Indeed, it is shown that discrete pure compaction bands are nucleated from local zones of porosity heterogeneity in the case of high-confining pressure, similarly to what is reported by Huang et al. (2019) and Chen et al. (2020). As for the deformation bands identified near the sample boundaries, the analyses of the kinematics of deformation have shown the presence of a significant shear component induced by the contrast of stiffness between the sample and the experimental device. At lower confining pressures, shear bands seem to be triggered by boundary effects.

The compaction band thicknesses measured on the DVC maps are of the order of few millimeters (see Figure 14). It is observed that the band thicknesses are mainly controlled by the length scale of the porosity heterogeneity, rather than the grain or pore scale (which is, in our case, lower than 250 μm). This result is in agreement with the observations made by Chen et al. (2020) on a high-porosity limestone. This observation is different from what is observed in sandstones for which the compaction band thickness is mainly controlled by the grain size as reported by Vajdova and Wong (2003); Tembe et al. (2006). However, the porosity reduction inside compaction bands obtained for Saint-Maximin limestone (between 10 to 15%) is comparable to the values reported by Sulem and Ouffroukh (2006) for compactive shear bands formed on a high-porosity sandstone.

Vajdova et al. (2010) and Ji et al. (2012) have observed a pore collapse mechanism involved in compaction banding in Tavel and Indiana limestones, respectively. In such a mechanism, larger pores collapse at first. However, this is not the case for Saint-Maximin limestone for which calcite grain crushing is identified. The reason that lays behind this difference is the variety of limestones microstructures. In a matrix-supported limestone (following the Dunham (1962) classification for carbonate rocks), as Tavel and Indiana limestones, stresses are concentrated around the pores. This induces a pore collapse mechanism which is reflected by the observed cataclastic damage around the pores. Therefore, the largest pores would collapse at first. However, in grain-supported limestones, stresses are concentrated at the grain contacts which can induce grain crushing as observed for Saint-Maximin limestone.

The experimental observations in the present study clearly establish the predominant role of the spatial distribution at centimetric scale of the low- and high-porosity zones in the sample on the heterogeneity of the local strain at millimetric scale. In order to model numerically the observed localization modes, it sounds thus of primary importance to take into account the major geometric features of this porosity distribution at mesoscale. A possible approach would be to provide an explicit geometric information on the spatial distribution of the porosity as an input to a full-field type of numerical simulation of a sample under given boundary conditions. Such geometric information might be directly provided by experimental porosity maps such a those computed in the present study from the XRCT data; they might also be generated virtually by some morphological model based on geometric parameters turned to be representative of the rock. On the other hand, in view of reducing the cost of numerical simulations, one might prefer an alternative approach, in which the details of the geometric features of a particular sample are not explicitly described. Owing to the absence of separation of the length scale of the sample (4cm) and of the geometric features of the compaction bands (mm to cm), non-local macroscopic approaches should then be considered with constitutive properties taking into account the scale of the spatial distribution of the porosity. The development of a constitutive model based on gradient-dependent plasticity theory, making use not only of the local porosity at a material point but also of its gradients (Vardoulakis and Sulem, 1995), its calibration and its implementation in a finite element code is actually the purpose of the companion paper (Abdallah et al., 2020).

This study focuses on compaction banding in dry conditions. However, it

has been recognized that water severely weakens the mechanical properties of many sedimentary rocks, such as the Saint-Maximin limestone. Therefore, the study will be extended to saturated conditions in a near future. On the other hand, a high-porosity rock has been studied to make evidence of compaction bands formation. More generally, the proposed methodology can be used to explore the role of the microstructure in the formation of deformation bands in other rock types.

A Estimation of the Uncertainties on the Strain Field Computation from the DVC Analysis

To evaluate the DVC strain field uncertainties and assess the order of magnitude of the errors, the DVC technique is applied on the reference sample. The microstructure and geometry of the reference sample remains unchanged for all XRCT observations. Ideally, a zero deformation tensor should be obtained for all the elements, as well as for the average strain. Figure 19 shows typical volumetric strain and shear strain magnitude maps obtained for the reference sample. The maximum local volumetric strain and shear strain magnitude (averaged over an element) are both in the order of 0.5%. 90% of the volumetric strain errors range between -1.35 $\times$ 10^{-3} and 1.35 $\times$ 10^{-3}. In addition, 90% of the shear strain magnitude values are lower than 3.48 $\times$ 10^{-3}. An average of the strain tensor components over all the elements of the mesh permits to assess the error of the global deformation measured over the reference sample (Equation 4). The mean volumetric deformation is thus $\langle \epsilon_v \rangle = \mathrm{Tr}(\langle \underline{\underline{\epsilon}} \rangle) = 2.16 \times 10^{-4}$, whereas the mean shear strain magnitude is $\langle \gamma \rangle = \sqrt{2\langle \underline{\underline{e}} \rangle : \langle \underline{\underline{e}} \rangle} = 2.74 \times 10^{-4}$. From these analyses, one can conclude that the order of magnitude of the error on the deformation field obtained from the DVC evaluated for a local gauge length of 40 voxels or $\simeq$ 1 mm, is in the order of 10^{-3}. For average strains over volumes with same diameters than the sample, the accuracy is one order of magnitude better.

$$\langle \underline{\underline{\epsilon}} \rangle = \begin{bmatrix} 0.56 & 0.35 & -0.68 \\ 0.35 & 0.67 & -1.12 \\ -0.68 & -1.12 & 0.93 \end{bmatrix} \times 10^{-4} \tag{4}$$

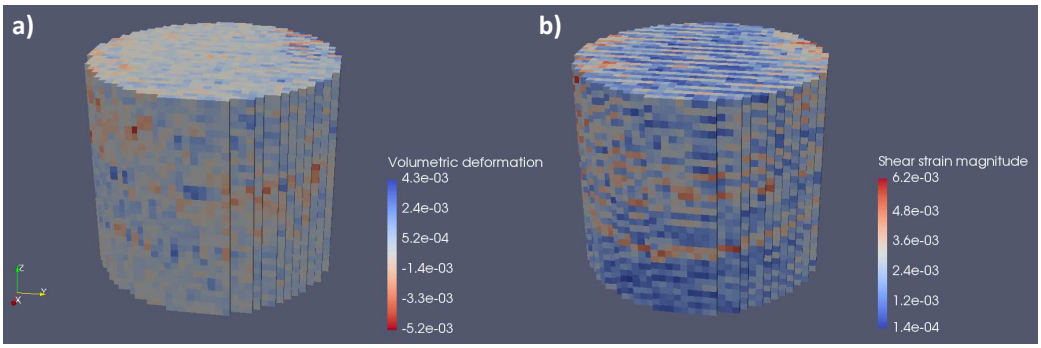

Figure 19: Typical local strain field obtained when DVC is applied on the reference sample: **(a)** Volumetric deformation map; **(b)** Shear strain magnitude map.

Note that errors on local strain are primarily induced by image noise, while for average strains, they may in addition be induced by the evolution of the geometric parameters of the tomography setup. Owing to their limited amplitude, it was however decided not to correct the results for such variations.

B Quartz and Calcite Absorption Coefficients

The Beer-Lambert law (Equation 5) relates the incident intensity I_0 of a X-ray beam to the transmitted intensity $I(x)$ through a pure material of length x and linear attenuation coefficient μ:

$$I(x) = I_0 \exp(-\mu x) \tag{5}$$

The XRCT observations are performed at a source energy of 100 kV. The transmittance coefficients $e^{-\mu.x}$ of pure quartz and calcite minerals with respect to the source energy for a material length of $x = 0.96$ mm are depicted in Figure 20, where the effect of the copper filter is taken into account. The attenuation coefficients of both pure phases, calcite and quartz, as well as for copper can be found on the NIST (2019). The choice of the length x corresponds to the diameter of the subvolume over which the porosity is evaluated. Therefore, it is observed that the variability of the local mineral proportion has a negligible effect on the homogenized solid matrix grey

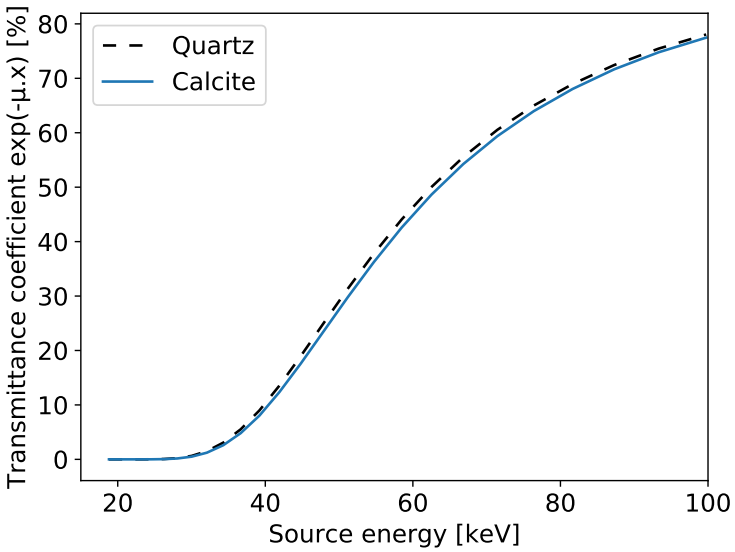

Figure 20: Transmittance coefficient evolution with respect to the source energy over a material length of 0.96 mm for both quartz and calcite minerals, taking into account the 0.5 mm copper filter (which stops X-rays below around 30 kV).

value (which is proportional to the absorption coefficient). Hence, an assumption can be made on the grey values of quartz and calcite, such as: $g_{\text{calcite}} \simeq g_{\text{quartz}} \simeq g_{\text{solid phase}}$, where $g_{\text{solid phase}}$ corresponds to the grey level of the homogenized solid matrix.

References

Abdallah, Y., 2019. Compaction banding in high-porosity carbonate rocks: Experimental observations and modelling. Phd dissertation. Université Paris-Est, Marne-la-Vallée, France.

Abdallah, Y., Sulem, J., Stefanou, I., 2020. Compaction banding in high-porosity carbonate rocks. Part II: A gradient-dependent plasticity model. Journal of Geophysical Research Submitted for publication.

Ayachit, U., 2015. The paraview guide: a parallel visualization application. Kitware, Inc.

Aydin, A., Borja, R.I., Eichhubl, P., 2006. Geological and mathematical framework for failure modes in granular rock. Journal of Structural Geology 28, 83–98. doi:https://doi.org/10.1016/j.jsg.2005.07.008.

Baechle, G.T., Colpaert, A., Eberli, G.P., Weger, R.J., 2008. Effects of microporosity on sonic velocity in carbonate rocks. The Leading Edge 27, 1012–1018.

Barbier, E., 2002. Geothermal energy technology and current status: an overview. Renewable and Sustainable Energy Reviews 6, 3–65. doi:https://doi.org/10.1016/S1364-0321(02)00002-3.

Baud, P., Exner, U., Lommatzsch, M., Reuschlé, T., Wong, T.f., 2017b. Mechanical behavior, failure mode, and transport properties in a porous carbonate. Journal of Geophysical Research: Solid Earth 122, 7363–7387. doi:https://doi.org/10.1002/2017jb014060.

Baud, P., Klein, E., Wong, T.f., 2004. Compaction localization in porous sandstones: spatial evolution of damage and acoustic emission activity. Journal of Structural Geology 26, 603–624. doi:https://doi.org/10.1016/j.jsg.2003.09.002.

Baud, P., Schubnel, A., Heap, M., Rolland, A., 2017a. Inelastic compaction in high-porosity limestone monitored using acoustic emissions. Journal of Geophysical Research: Solid Earth 122, 9989–10,008. doi:https://doi.org/10.1002/2017JB014627.

Baud, P., Vinciguerra, S., David, C., Cavallo, A., Walker, E., Reuschlé, T., 2009. Compaction and failure in high porosity carbonates: Mechanical data and microstructural observations. Pure and Applied Geophysics 166, 869–898. doi:https://doi.org/10.1007/s00024-009-0493-2.

Bay, B.K., Smith, T.S., Fyhrie, D.P., Saad, M., 1999. Digital volume correlation: three-dimensional strain mapping using x-ray tomography. Experimental mechanics 39, 217–226.

Bornert, M., Chaix, J.M., Doumalin, P., Dupré, J.C., Fournel, T., Jeulin, D., Maire, E., Moreaud, M., Moulinec, H., 2004. Mesure tridimensionnelle de champs cinématiques par imagerie volumique pour l'analyse des matériaux et des structures. Instrumentation, Mesure, Métrologie 4, 43–88.

Chen, X., Roshan, H., Lv, A., Hu, M., Regenauer-Lieb, K., 2020. The dynamic evolution of compaction bands in highly porous carbonates: the role of local heterogeneity for nucleation and propagation. Progress in Earth and Planetary Science 7, 1–19.

Cheung, C.S., Baud, P., Wong, T.f., 2012. Effect of grain size distribution on the development of compaction localization in porous sandstone. Geophysical Research Letters 39. doi:https://doi.org/10.1029/2012GL053739.

Choquette, P.W., Pray, L.C., 1970. Geologic nomenclature and classification of porosity in sedimentary carbonates. AAPG bulletin 54, 207–250. doi:https://doi.org/10.1306/5D25C98B-16C1-11D7-8645000102C1865D.

Ciantia, M., Hueckel, T., 2013. Weathering of submerged stressed calcarenites: chemo-mechanical coupling mechanisms. Géotechnique 63, 768–785. doi:https://doi.org/10.1680/geot.SIP13.P.024.

Dautriat, J., Bornert, M., Gland, N., Dimanov, A., Raphanel, J., 2011. Localized deformation induced by heterogeneities in porous carbonate analysed by multi-scale digital image correlation. Tectonophysics 503, 100–116.

Dunham, R.J., 1962. Classification of carbonate rocks according to depositional textures. AAPG Special Volumes.

Eichhubl, P., Hooker, J.N., Laubach, S.E., 2010. Pure and shear-enhanced compaction bands in aztec sandstone. Journal of Structural Geology 32, 1873–1886. doi:https://doi.org/10.1016/j.jsg.2010.02.004.

Feldkamp, L.A., Davis, L., Kress, J.W., 1984. Practical cone-beam algorithm. Josa a 1, 612–619. doi:https://doi.org/10.1364/JOSAA.1.000612.

Flügel, E., 2013. Microfacies of carbonate rocks: analysis, interpretation and application. Springer Science & Business Media.

Follet, H., Bruyère-Garnier, K., Peyrin, F., Roux, J.P., Arlot, M., Burt-Pichat, B., Rumelhart, C., Meunier, P., 2005. Relationship between compressive properties of human os calcis cancellous bone and microarchitecture assessed from 2d and 3d synchrotron microtomography. Bone 36, 340–351. doi:https://doi.org/10.1016/j.bone.2004.10.011.

Fortin, J., Stanchits, S., Dresen, G., Guéguen, Y., 2006. Acoustic emission and velocities associated with the formation of compaction bands in sandstone. Journal of Geophysical Research: Solid Earth 111. doi:https://doi.org/10.1029/2005JB003854.

Fossen, H., Schultz, R.A., Torabi, A., 2011. Conditions and implications for compaction band formation in the navajo sandstone, utah. Journal of Structural Geology 33, 1477–1490. doi:https://doi.org/10.1016/j.jsg.2011.08.001.

Fronteau, G., Moreau, C., Thomachot-Schneider, C., Barbin, V., 2010. Variability of some lutetian building stones from the paris basin, from characterisation to conservation. Engineering Geology 115, 158–166. doi:https://doi.org/10.1016/j.enggeo.2009.08.001.

Gaye, A., 2015. Analyse multiéchelle des mécanismes de déformation du sel gemme par mesures de champs surfaciques et volumiques. PhD dissertation. Université Paris Est, Marne-la-Vallée, France.

Grgic, D., 2011. Influence of CO2 on the long-term chemomechanical behavior of an oolitic limestone. Journal of Geophysical Research: Solid Earth 116. doi:https://doi.org/10.1029/2010JB008176.

Hill, R., 1962. Acceleration waves in solids. Journal of the Mechanics and Physics of Solids 10, 1–16. doi:https://doi.org/10.1016/0022-5096(62)90024-8.

Holcomb, D., Rudnicki, J.W., Issen, K.A., Sternlof, K., 2007. Compaction localization in the earth and the laboratory: state of the research and research directions. Acta Geotechnica 2, 1–15. doi:https://doi.org/10.1007/s11440-007-0027-y.

Huang, L., Baud, P., Cordonnier, B., Renard, F., Liu, L., Wong, T.f., 2019. Synchrotron x-ray imaging in 4d: Multiscale failure and compaction localization in triaxially compressed porous limestone. Earth and Planetary Science Letters 528, 115831.

Ji, Y., Baud, P., Vajdova, V., Wong, T.f., 2012. Characterization of pore geometry of indiana limestone in relation to mechanical compaction. Oil & Gas Science and Technology–Revue dIFP Energies nouvelles 67, 753–775.

Ji, Y., Hall, S.A., Baud, P., Wong, T.f., 2014. Characterization of pore structure and strain localization in majella limestone by x-ray computed tomography and digital image correlation. Geophysical Journal International 200, 701–719. doi:https://doi.org/10.1093/gji/ggu414.

Lenoir, N., Bornert, M., Desrues, J., Bésuelle, P., Viggiani, G., 2007. Volumetric digital image correlation applied to X-ray microtomography images from triaxial compression tests on argillaceous rock. Strain 43, 193–205. doi:https://doi.org/10.1111/j.1475-1305.2007.00348.x.

NIST, 2019. Website of the national institute of standards and technology. https://physics.nist.gov/PhysRefData/FFast/html/form.html.

Olsson, W., Holcomb, D., Rudnicki, J., 2002. Compaction localization in porous sandstone: Implications for reservoir mechanics. Oil & Gas Science and Technology 57, 591–599. doi:https://doi.org/10.2516/ogst:2002040.

Otani, J., Mukunoki, T., Sugawara, K., 2005. Evaluation of particle crushing in soils using x-ray ct data. Journal of the Japanese Geotechnical Society: Soils and Foundation 45, 99–108. doi:https://doi.org/10.3208/sandf.45.1_99.

Papazoglou, A., Shahin, G., Marinelli, F., Dano, C., Buscarnera, G., Viggiani, G., 2017. Localized compaction in tuffeau de maastricht: Experiments and modeling, in: Bifurcation and Degradation of Geomaterials with Engineering Applications, E. Papamichos, P. Papanastasiou, E. Pasternak, A. Dyskin (eds), Springer. pp. 481–488. doi:https://doi.org/10.1007/978-3-319-56397-8_61.

Rath, A., Exner, U., Tschegg, C., Grasemann, B., Laner, R., Draganits, E., 2011. Diagenetic control of deformation mechanisms in deformation bands in a carbonate grainstone. AAPG bulletin 95, 1369–1381. doi:https://doi.org/10.1306/01031110118.

Rudnicki, J.W., Rice, J., 1975. Conditions for the localization of deformation in pressure-sensitive dilatant materials. Journal of the Mechanics and Physics of Solids 23, 371–394. doi:10.1016/0022-5096(75)90001-0.

Rustichelli, A., Tondi, E., Agosta, F., Cilona, A., Giorgioni, M., 2012. Development and distribution of bed-parallel compaction bands and pressure solution seams in carbonates (Bolognano Formation, Majella Mountain, Italy). Journal of Structural Geology 37, 181–199. doi:https://doi.org/10.1016/j.jsg.2012.01.007.

Rutqvist, J., 2012. The geomechanics of CO2 storage in deep sedimentary formations. Geotechnical and Geological Engineering 30, 525–551. doi:10.1007/s10706-011-9491-0.

Schindelin, J., Arganda-Carreras, I., Frise, E., Kaynig, V., Longair, M., Pietzsch, T., Preibisch, S., Rueden, C., Saalfeld, S., Schmid, B., et al., 2012. Fiji: an open-source platform for biological-image analysis. Nature Methods 9, 676–682. doi:https://doi.org/10.1038/nmeth.2019.

Stefanou, I., Sulem, J., 2014. Chemically induced compaction bands: Triggering conditions and band thickness. Journal of Geophysical Research: Solid Earth 119, 880–899. doi:https://doi.org/10.1002/2013JB010342.

Sternlof, K.R., Rudnicki, J.W., Pollard, D.D., 2005. Anticrack inclusion model for compaction bands in sandstone. Journal of Geophysical Research: Solid Earth 110. doi:https://doi.org/10.1029/2005JB003764.

Sulem, J., Ouffroukh, H., 2006. Shear banding in drained and undrained triaxial tests on a saturated sandstone: Porosity and permeability evolution. International Journal of Rock Mechanics and Mining Sciences 43, 292–310.

Tembe, S., Vajdova, V., Wong, T.f., Zhu, W., 2006. Initiation and propagation of strain localization in circumferentially notched samples of two porous sandstones. Journal of Geophysical Research: Solid Earth 111.

Tondi, E., Antonellini, M., Aydin, A., Marchegiani, L., Cello, G., 2006. The role of deformation bands, stylolites and sheared stylolites in fault development in carbonate grainstones of Majella Mountain, Italy. Journal of structural geology 28, 376–391. doi:https://doi.org/10.1016/j.jsg.2005.12.001.

Vajdova, V., Baud, P., Wong, T.f., 2004. Compaction, dilatancy, and failure in porous carbonate rocks. Journal of Geophysical Research: Solid Earth 109. doi:https://doi.org/10.1029/2003JB002508.

Vajdova, V., Wong, T.F., 2003. Incremental propagation of discrete compaction bands: Acoustic emission and microstructural observations on circumferentially notched samples of bentheim. Geophysical Research Letters 30.

Vajdova, V., Zhu, W., Chen, T.M.N., Wong, T.f., 2010. Micromechanics of brittle faulting and cataclastic flow in tavel limestone. Journal of Structural Geology 32, 1158–1169.

Vardoulakis, I., Sulem, J., 1995. Bifurcation analysis in geomechanics.

Wong, T.f., Baud, P., 2012. The brittle-ductile transition in porous rock: A review. Journal of Structural Geology 44, 25–53. doi:https://doi.org/10.1016/j.jsg.2012.07.010.

Wong, T.f., David, C., Zhu, W., 1997. The transition from brittle faulting to cataclastic flow in porous sandstones: Mechanical deformation. Journal of Geophysical Research: Solid Earth 102, 3009–3025. doi:https://doi.org/10.1029/96JB03281.

Wu, H., Zhao, J., Liang, W., 2020. The signature of deformation bands in porous sandstones. Rock Mechanics and Rock Engineering , 1–15doi:https://doi.org/10.1007/s00603-020-02100-8.

Wu, X.Y., Baud, P., Wong, T.f., 2000. Micromechanics of compressive failure and spatial evolution of anisotropic damage in darley dale sandstone. International Journal of Rock Mechanics and Mining Sciences 37, 143–160. doi:https://doi.org/10.1016/S1365-1609(99)00093-3.

Zhu, W., Baud, P., Wong, T.f., 2010. Micromechanics of cataclastic pore collapse in limestone. Journal of Geophysical Research: Solid Earth 115. doi:https://doi.org/10.1029/2009JB006610.

Zinsmeister, L., 2013. Étude de l'évolution hydromécanique d'un carbonate après altération chimique. Application des méthodes de corrélation d'images 2D et 3D à la mesure des champs locaux de déformation lors d'essais mécaniques à différentes échelles. Phd dissertation. Ecole polytechnique, Palaiseau, France.